

The behaviour of beach elevation contours in response to different wave energy environments

Wenhong Pang,¹ Zhenpeng Ge,¹ Zhijun Dai,^{1,2*}  Shushi Li³ and Hu Huang³

¹ State Key Laboratory of Estuarine & Coastal Research, East China Normal University, Shanghai, China

² Laboratory for Marine Geology, Qingdao National Laboratory for Marine Science and Technology, Qingdao 266061, China

³ Key Laboratory of Coastal Science and Engineering, Beibu Gulf University, Qinzhou, China

Received 6 September 2020; Revised 3 November 2020; Accepted 8 November 2020

*Correspondence to: Zhijun Dai, State Key Laboratory of Estuarine and Coastal Research, East China Normal University, Shanghai, China.

E-mail: zjdai@sklec.ecnu.edu.cn

ESPL

Earth Surface Processes and Landforms

ABSTRACT: Within the context of a warming climate, there are wide and increasing concerns about the way beaches respond to different wave energy environments. However, behavioural differences in changes in beach elevation contours (including shorelines) in different wave energy environments remain unknown. Thus, it is unilateral to evaluate the changes in beaches based on a single elevation contour (e.g. shoreline) in coastal engineering and management applications. In this study, based on the collected shoreline and wave energy data of two international beaches, as well as the measured beach elevation contour data from Yintan Beach and the corresponding wave energy data simulated by Xbeach, our results show that frequency distributions of beach elevation contour changes exhibit distinct features under different wave energy environments. Under high wave energy environments, the frequency distributions of beach elevation contour changes show a Gaussian distribution. However, frequency distributions of beach elevation contour changes present a power law, intermediate between the logarithmic and Gaussian distributions under low and moderate wave energy environments, respectively. Furthermore, the conceptual model of beach elevation contour changes constructed by this study indicates that the relative importance of the wave energy and sediment resistance determines this phenomenon. © 2020 John Wiley & Sons Ltd

KEYWORDS: meso-macrotidal beach; beach elevation contour; wave energy environment; morphodynamic; extreme event

Introduction

Beaches act as important entertainment venues, harbours, and aquaculture (Nordstrom, 2000), which have unique ecological resources and provide valuable habitats for organisms worldwide (Defeo *et al.*, 2009). In particular, beaches serve as the first defence via a shoreline retreat to protect life and property from the damage of strong waves, especially storm waves, in coastal cities (Stive, 2004; Anthony, 2008). Most studies indicate that the shoreline position represents a 'beach vulnerability indicator' for studying and evaluating both the long-term (decades or longer) and short-term (e.g. the timescale of individual typhoon events) beach evolution (Kroon *et al.*, 2007; Dawson and Smithers, 2010; Hinkel *et al.*, 2015; Bonaldo *et al.*, 2019). However, generalized shorelines (i.e. elevation contours) are usually applied to mainly study beach volume changes (Smith and Bryan, 2007; Quartel *et al.*, 2008), and little information is relevant to the identification of how beach elevation contours respond to different wave energy environments, which is vital to understanding beach morphodynamics.

With the understanding that different wave energy environments, which have a substantial influence on the shoreline, are not negligible for long-term trends of shoreline evolution (Anderson *et al.*, 2010), researchers have paid close attention to shoreline behaviours under different wave conditions via a

variety of survey tools (e.g. Autonomous Real-Time Ground Ubiquitous Surveillance Imaging System [ARGUS-IS]; Lippmann and Holman, 1989). It is well established that a single typical contour (i.e. shoreline) of beach terrain is often incapable of detecting how the whole beach face responds to different wave environments (Boak and Turner, 2005; Theuerkauf and Rodriguez, 2014). Archetti and Romagnoli (2011) also demonstrated that the understanding of the behaviour of one typical contour (e.g. the mean high water level of spring tide for a shoreline) in response to hydrodynamic conditions does not reflect realistic coastal morphodynamic evolution. Beach accretion/erosion often has obvious heterogeneity in different beach zones. Thus, the evolutions of elevation contours in different beach zones are more representative of beach morphodynamics when beach topographical variations from low to high intertidal zones are taken into account (Short, 1979).

Although shoreline changes in beaches have been widely investigated, many processes remain unknown since the complexity of shoreline changes is often neglected (Splinter *et al.*, 2017). While numerous studies have focused on modelling shoreline evolution based on the physical process or equilibrium concept (e.g. Ashton *et al.*, 2001; Yates *et al.*, 2009), little information with respect to beach elevation contour changes and the corresponding frequency distributions

has been acquired. In the sense of statistics, different frequency distributions of beach shoreline/contour changes indicate distinct mechanisms behind shoreline evolution (Leonardi and Fagherazzi, 2014, 2015). Hence, it is essential and urgent to explore the different frequency distributions to advance our understanding of the roles of hydrodynamic environments and sediment characteristics in shoreline/contour evolution. With the further understanding of the behaviour of beach elevation contours, more flexible and economic coastal management strategies could be formulated and applied for different beach zones with different wave environments (Yu *et al.*, 2013).

To approach the above purpose, high spatial resolution terrain data collected by LiDAR in Yintan, China were analysed. In addition, shoreline data collected by ARGUS-IS in Lido di Dante, Italy and Egmond, North Holland were obtained from historical literature (Aagaard *et al.*, 2005; Archetti and Romagnoli, 2011). The elevation contour/shoreline changes of these three beaches in stormy conditions were examined. In addition, we took a novel step forward by constructing a unique conceptual model. The main goals of this paper are to analyse the different frequency distributions of beach elevation contour/shoreline changes under different wave energy environments and to explore the mechanisms behind this phenomenon with a new conceptual model. This study enhances the understanding of the mechanism of beach morphological evolution, which is of great importance for coastal engineering, protection and management applications.

Materials and Methods

Study areas

Yintan Beach is north of Beibu Gulf (Figures 1A–C). The beach is characterized by mixed diurnal–semidiurnal tides with a mean tidal range of 2.3 m and a maximum tidal range of 5.36 m, so it is considered a meso-macrotidal beach. The typical wave climate is characterized by a mean wave height of approximately 0.5 m and wave directions of N–NE in autumn through spring, and SW–S in summer. The beach has a relatively flat beach face (the average slope is 0.02; Figure 1E) and a small coastal dune with a relatively large intertidal sandbar located in the swash zone (Figure 1D). The beach is composed of fine sand with a median grain size of 0.14 mm.

Typhoon Rammasun was the most severe typhoon affecting south China in the past 40 years in the Beibu Gulf. Typhoon Rammasun (tropical storm no. 1409) formed on 12 July 2014 in the northwest Pacific Ocean with an initial wind speed of 18 m s^{-1} . It moved northwest from the Pacific Ocean towards China and Vietnam with a minimum central pressure of 899.2 hPa and a maximum wind speed of 72 m s^{-1} . Typhoon Rammasun was the most violent typhoon that has affected Yintan Beach in the past 40 years and passed the beach from 18 to 20 July with an average speed of approximately 50 m s^{-1} (Figure 1B; Ge *et al.*, 2017). Due to the impact of Rammasun, there was an obvious storm surge with a mean and maximum amplitude of over 0.7 and 1.7 m, respectively.

Lido di Dante is an artificial beach in northeast Italy (Figures 1F and G; Archetti and Romagnoli, 2011). It is a microtidal beach with a tidal range from 0.15 cm during neap to 0.4 m during spring. Wave conditions are commonly characterized by a 0.5 m significant wave height, a 3.5–4.0 s wave period, and either a NE or a SE wave direction. Egmond is on the Central Dutch coast in North Holland (Figures 1H and I; Aagaard *et al.*, 2005). The mean semidiurnal tidal range of this area is 1.65 m, and the tidal range increases to 2.1 m at spring tide. The mean annual offshore wave climate features a significant wave height of approximately 1.2 m, wave periods of 5 s, and a wave direction of SW to N.

Terrain data and analysis

For Yintan Beach, a LiDAR survey with an area of approximately 300 m in the cross-shore direction and 500 m in the alongshore direction was conducted before the typhoon on 17 July 2014 and after the typhoon on 20 July 2014 (Ge *et al.*, 2017). Digital elevation models (DEMs) with a high spatial resolution of 25 mm were extracted from elevation points. Typical contours, including -1.5 , -1 , -0.5 , -0.3 , and 0 m, were extracted from DEMs for both days (Figures 2A–E). Among these contours (Figure 1E), the -1.5 and -1 m contours were located in the foreshore and were in the surf zone of this beach, while the -1 m contour was close to a sandbar (Figures 2A and B). The -0.5 and -0.3 m contours were located in the swash zone of this beach where a sandbar developed in this zone (Figures 2C and D); the 0 m contour was

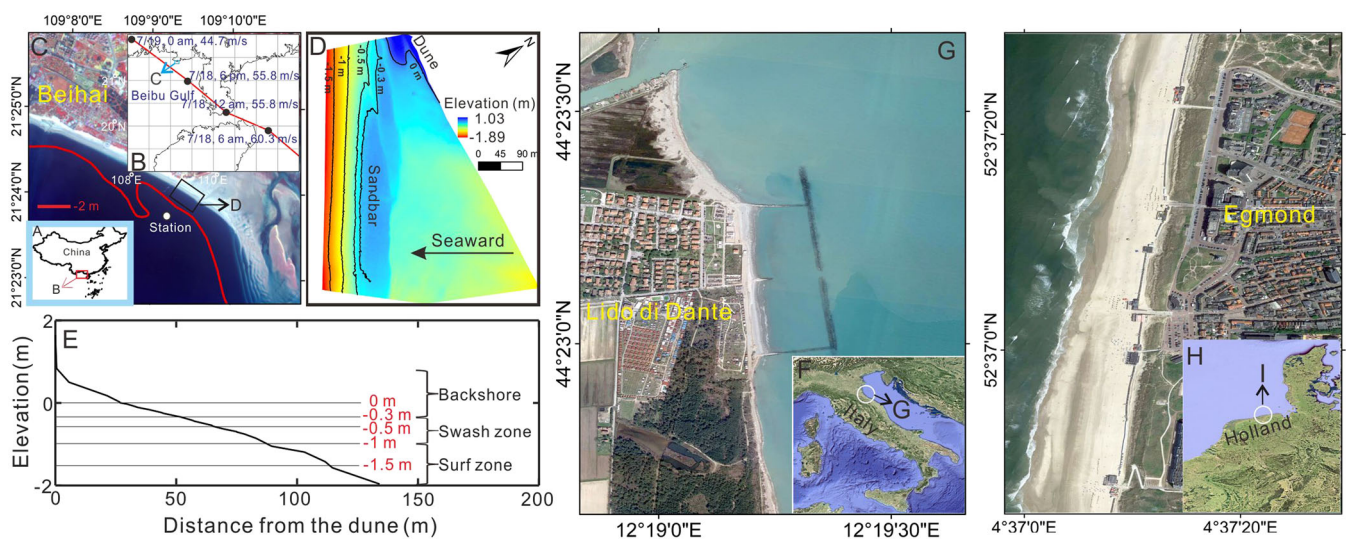


Figure 1. The study region: (A) the location of Yintan Beach; (B) the track (red line) and the centre (black solid circle) of Typhoon Rammasun; (C) remote sensing image for Yintan Beach and adjacent areas; (D) DEM of the study region of Yintan Beach on 17 July 2014; (E) a typical profile in the study region; (F, G) the location of Lido di Dante; (H, I) the location of Egmond.

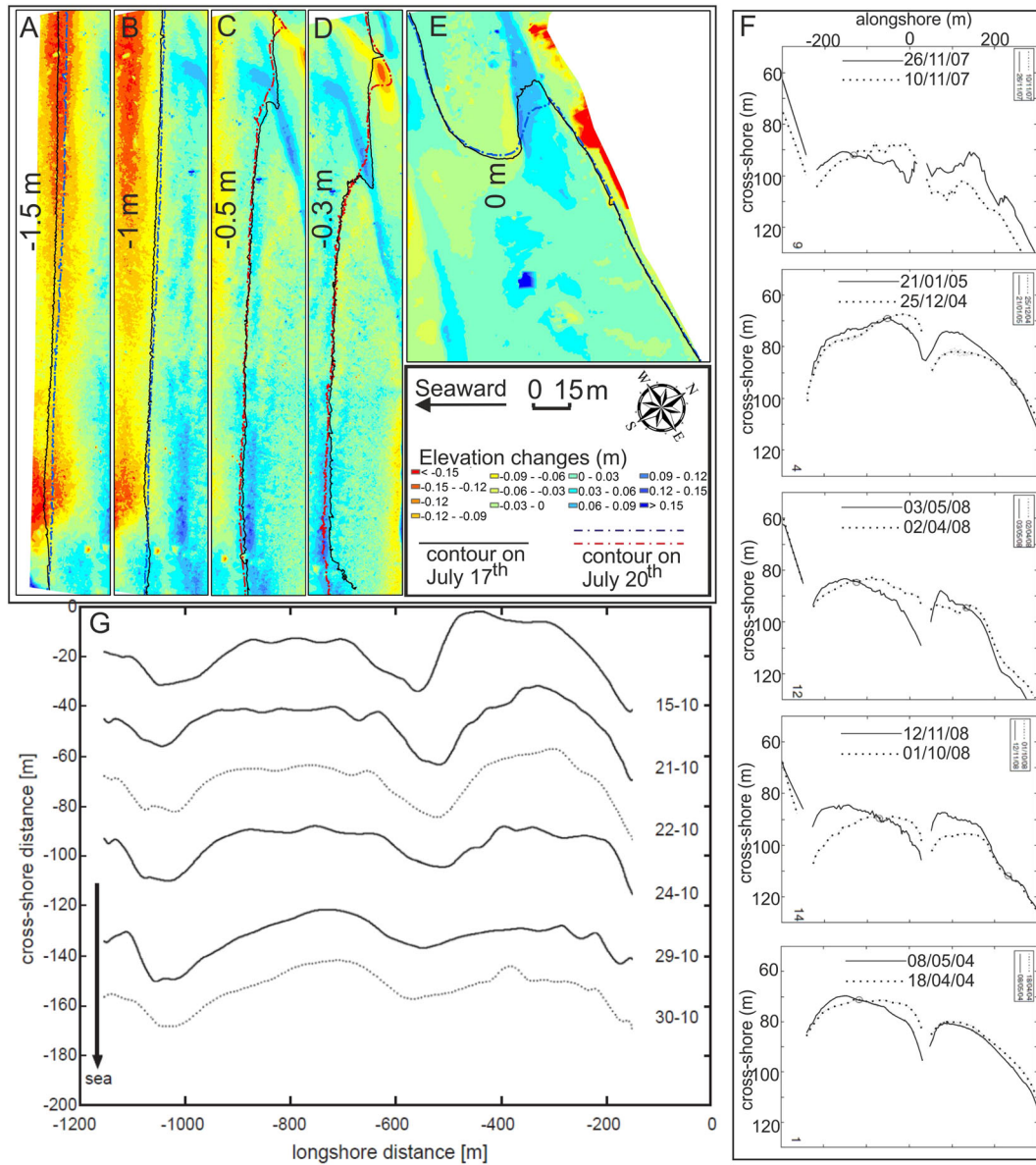


Figure 2. Contours of three beaches: (A–E) identical contours before and after Typhoon Rammasan in Yintan Beach; (F) identical shorelines before and after different storm events in Lido di Dante (figure modified from Archetti and Romagnoli, 2011); (G) identical shorelines from different days in Egmond (figure modified from Aagaard *et al.*, 2005) and the shoreline shifted by 25 m in the cross-shore direction between each time step.

located in the backshore of this beach and was close to the foot of the dune (Figure 2E).

For Lido di Dante Beach and Egmond Beach, the shorelines (in Table I, the zero level referred to the local mean sea water level for Lido di Dante, and -0.6 m referred to that of NAP for Egmond Beach, respectively) were measured by ARGUS-IS. These shorelines were digitized from Archetti and Romagnoli (2011) and Aagaard *et al.* (2005), respectively. We

obtained five pairs of shorelines pre and post five southern storm (Sirocco winds from southeast direction) conditions at Lido di Dante (Figure 2F; Archetti and Romagnoli, 2011), and six shorelines in October 2002 at Egmond (Figure 2G; Aagaard *et al.*, 2005).

Digital Shoreline Analysis System (DSAS) software version 4.3 was used to calculate the absolute spatial changes of the identical contours/shorelines (Thieler *et al.*, 2009). Specifically,

Table I. The locations and levels of the beach elevation contours used for comparison from three beaches (Aagaard *et al.*, 2005; Archetti and Romagnoli, 2011)

Beach	Contour level	Elevation datum	Location
Yintan Beach	0 m	Local mean high water level of spring tide	Close to the foot of sand dune (backshore)
	-0.3 m		In the swash zone
	-0.5 m		In the swash zone
	-1 m		In the surf zone
	-1.5 m		In the surf zone
Lido di Dante	Shoreline (zero level)	Local mean sea water level	In the surf zone
Egmond	Shoreline (-0.6 m NAP)	NAP (Normaal Amsterdams Peil)	In the breaker zone

a series of transect lines at intervals of 1 m were constructed from the baseline for the three beaches. Then, the advance/retreat distance of the identical contours for two days was determined by the distance between two cross points generated by a transect line and the two identical contours (Thieler *et al.*, 2009). Afterwards, the absolute values of these distances were sorted by size, and the number of these absolute values was counted at different partitioned intervals (full details on the partitioned intervals of the frequency distribution statistics referring to different contour changes from three beaches and the conceptual model are provided in Table S1 of the online Supporting Information), during which the partitioned interval was dependent on the specific condition of each case. Thus, the frequency of each partitioned interval was obtained by dividing its number by the total number of contour changes. For instance, the absolute changes and the corresponding frequency distribution of the Egmond shoreline between 15 and 21 October were calculated with a partitioned interval of 1 m (Figures 2G and 6O).

Xbeach model

Xbeach is a numerical model designed for estimating beach evolutions under typhoon events (Roelvink *et al.*, 2009). This model has been widely used in both engineering applications and scientific research (McCall *et al.*, 2010; Corbella and Stretch, 2012). It was utilized to obtain the wave energy for Yintan Beach. The hourly water level and wave data (significant wave height, spectral peak wave period, wave direction) collected at 8, 10 and 11 am, 12, 2, 4, 5 and 6 pm for each day during Typhoon Rammasun were used as boundary conditions in the model.

The survey area on Yintan Beach is the prototype of this model domain with an extension for obtaining better offshore boundary conditions and reducing the boundary effect of the eastern lateral boundary. A station was located approximately 500 m away from the survey area (Figure 1C), so the bathymetry data of the model domain were extended to the location of the wave buoy in the cross-shore direction, and the slopes were achieved from the nautical chart published by the navigation assurance department of the Chinese People's Liberation Army navy command. Furthermore, the eastern lateral boundary was extended approximately 300 m eastward in the alongshore direction with the slope obtained from the map published by SinoMaps Press.

The input of the storm surge data was interpolated into 2-min intervals with a linear method, while the input of the wave data (significant wave heights, spectral peak wave period, wave direction) remained uniform between the two measurements. This model was configured with a curvilinear grid of 301×301 cells, and the spatial resolution of the grid was approximately 0.8 m in the survey area and approximately 2.6 m in the other parts of the domain. The list of detailed parameters during the model setup is shown in Table II (the parameters were kept at the default settings in Xbeach if they did not appear in Table II).

With this model, the wave energy over the survey area during Typhoon Rammasun was obtained. To compare the variations in the wave energy environment for different contours, the polygon that was bounded by the identical contours (e.g. -1.5 m contour) pre- and post-typhoon was quantitatively defined as the region of interest. The average wave energy per cell (AWEPC) based on the model results was calculated for the entire simulation period (Figure 4C).

Table II. The list of model parameters (an explanation for each parameter can be found in the Xbeach manual at http://xbeach.readthedocs.io/en/latest/user_manual.html)

Parameter	Value	Parameter	Value
D_{50}	0.00013	gridform	delft3d
D_{90}	0.00025	tstop	68,400
front	abs_2d	morfac	10
back	abs_2d	wetslp	0.3
posdwn	1	dryslp	1
alfa	0	tideloc	2
thetamin	115	paulverre	sea
thetamax	235	instat	jons
dtheta	20	nmax	0.5

Estimation of sediment mobility number and wave friction factor

The sediment mobility number (ψ), as the ratio of the driving force to the resisting force on the sands over the seabed, is usually used to represent the dynamics of the bottom boundary layer and bedform morphology (Dingler and Inman, 1976; Nielsen, 1981). The mobility number is defined as:

$$\psi = \frac{U_m^2}{(s-1)gD_{50}} \quad (1)$$

where $s = 2.65$ is the specific density of sand, and U_m and D_{50} are the maximum wave orbital velocity and median grain size, respectively. U_m is calculated as:

$$U_m = (\pi H/T) \sinh(2\pi h/L) \quad (2)$$

where T is the wave period, h is the water depth, H is the wave height from the Xbeach model, and L is the wavelength obtained by iterative computations through the linear wave dispersion relation:

$$L = \left(\frac{gT^2}{2\pi} \right) \tanh(2\pi h/L) \quad (3)$$

In addition, the wave friction factor (f_w), a variable that depicts the incident wave height damping from bottom sediment resistance due to the seabed roughness under near-bed wave orbital motions (Swart, 1974), is defined as:

$$f_w = \exp \left[5.213 \left(\frac{k_s}{A_0} \right)^{0.194} - 5.977 \right] \quad (4)$$

where k_s is the bed roughness height, which is estimated as $2.5D_{50}$ for a plane seabed (smooth bed) and is given by 4ξ for a rippled seabed, where ξ is the ripple height of the seabed and meets the empirical formula according to Nielsen (1981):

$$\frac{\xi}{A_0} = 21 \psi^{-1.85} \quad (5)$$

when ψ is larger than 10.

A_0 is the near-bed orbital semi-excursion, obtained by:

$$A_0 = \left(\frac{U_m T}{2\pi} \right) \quad (6)$$

The novel conceptual model

The evolution of a contour/shoreline is a ubiquitous phenomenon as a consequence of sediment transport from variable

directions, which can be decomposed simply into alongshore and cross-shore directions (Dean and Dalrymple, 2004). Following previous studies, cross-shore sediment transport can be treated as a competition between the local sediment resistance and wave erosive ability (Fagherazzi *et al.*, 2006), and the erosive ability is formulated as:

$$E = A(\tau_w - \tau_{cr}) = A\tau_w - A\tau_{cr} \quad (7)$$

where E is the erosion rate, A is a constant for proportionality, τ_w is the wave bottom shear stress, and τ_{cr} (corresponding to sediment resistance) is the critical shear stress for incipient motion. In general, τ_{cr} is simply treated as a constant or parameterized with a median grain size, but the concept of τ_{cr} comes from the mechanics of a single grain, which is directly expanded to represent mixed grains by using the median grain size. In our novel conceptual model of beach contour change $\left(\frac{\partial y}{\partial t}\right)$, the erosion ability of waves ($A\tau_w$), being replaced by b , is uniform along one contour for each scenario, while the sediment resistance ($A\tau_{cr}$), being substituted by $k_1\eta y$, evolves with the contour changes:

$$\frac{\partial y}{\partial t} = \varepsilon_1 \frac{\partial^2 y}{\partial x^2} + k_1 \eta y - b \quad (8)$$

$$\frac{\partial \eta}{\partial t} = \varepsilon_2 \frac{\partial^2 \eta}{\partial x^2} + k_2 \left| \frac{\partial y}{\partial x} \right| \eta \quad (9)$$

where x is the alongshore coordinate, y is the contour position, and η is the sediment resistance (equivalent to relative sediment elevation) which reflects the sediment resistance to wave erosion by the vertical changes of the surface sediment layer. A larger η represents a stronger sediment resistance. b is the erosive ability of the waves and is always larger than 0. b reflects the relative bed shear stress associated with the wave energy and water depth. The larger b is, the higher the wave energy environment. ε_1 and ε_2 are diffusion coefficients of the contour position and relative sediment elevation (sediment resistance), respectively. k_1 is an anti-erosion parameter for the contour position; k_2 is an erosion parameter for sediment elevation (sediment resistance), which is similar to the erosion parameter of Winterwerp and van Kesteren (2004). ε_1 , ε_2 , k_1 , k_2 are all positive. In Equation 8, the beach contour change $\left(\frac{\partial y}{\partial t}\right)$ is divided into cross-shore ($k_1\eta y - b$) and alongshore $\left(\varepsilon_1 \frac{\partial^2 y}{\partial x^2}\right)$ terms of

sediment transport, with the cross-shore term representing sediment advection motion and the alongshore term representing sediment diffusion motion. Specifically, the advection term $k_1\eta y - b$ originates from Equation 7, while the diffusion term is motivated by the GENESIS model (Kraus and Harikai, 1983). Equation 9 is formulated to reflect the change rate of sediment resistance $\left(\frac{\partial \eta}{\partial t}\right)$, which is decomposed into

advection $\left(k_2 \left| \frac{\partial y}{\partial x} \right| \eta\right)$ and diffusion $\left(\varepsilon_2 \frac{\partial^2 \eta}{\partial x^2}\right)$ terms. The advection term of sediment transport is proportional to the local sinuosity of a contour. Equations 8 and 9 are solved with a one-dimensional explicit Adams–Bashforth scheme for temporal derivatives and a finite-difference numerical scheme for spatial derivatives (Garnier *et al.*, 2006).

This conceptual model is simulated on a grid of 5000×1 cells; and a periodic boundary condition is used. The initial condition for y uses uniform values, adding small random perturbations, while that for η uses random values between 0 and 1. The maximum cross-shore erosion distance (Δy) is fixed to 15 m for all scenarios, which is close to the maximum contour change (15.4 m) in the field data. Moreover, the mean of η (mean sediment resistance, MSR) and the standard deviation of η (standard deviation of the sediment resistance, SSR) of all the cells in the final state are used to quantitatively represent the strength of the sediment resistance for each scenario.

Results

Hydrodynamic conditions in three regions

From the offshore station, Typhoon Rammasun passed Yintan Beach during a neap tide period with a maximum tide range of 2.4 m (Figure 3A), and influenced Yintan Beach with a maximum wave height ranging from 2.5 to 4 m and a mean wave period ranging from 4.9 to 6.3 s from midnight on 18 July to the morning of 20 July (Figures 1B and 3B). Based on the Xbeach simulation, the space–time distribution of the wave energy on the beach face was obtained during Typhoon Rammasun. A typical profile (HP in Figure 4A) of the wave energy and three typical points along it were selected for presentation (S1, S2, S3 in Figure 4A). S1 featured an elevation of -1.3 m, which is located between the -1.5 and -1 m contours, and represents the surf zone of the beach during Typhoon Rammasun; S2 featured an elevation of -0.33 m, which is located between the -0.5 and -0.3 m contours, and represents the swash zone of the beach; S3 featured an elevation of -0.02

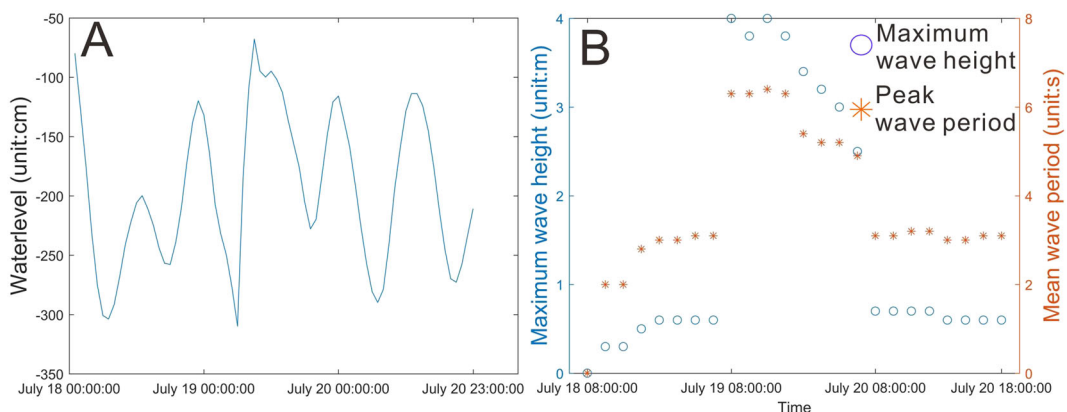


Figure 3. Hydrodynamic condition of a station (the station is shown as a white point in Figure 1C) near the study region in Yintan Beach during Typhoon Rammasun: (A) time series of the offshore water level; (B) time series of the offshore maximum wave height and mean wave period.

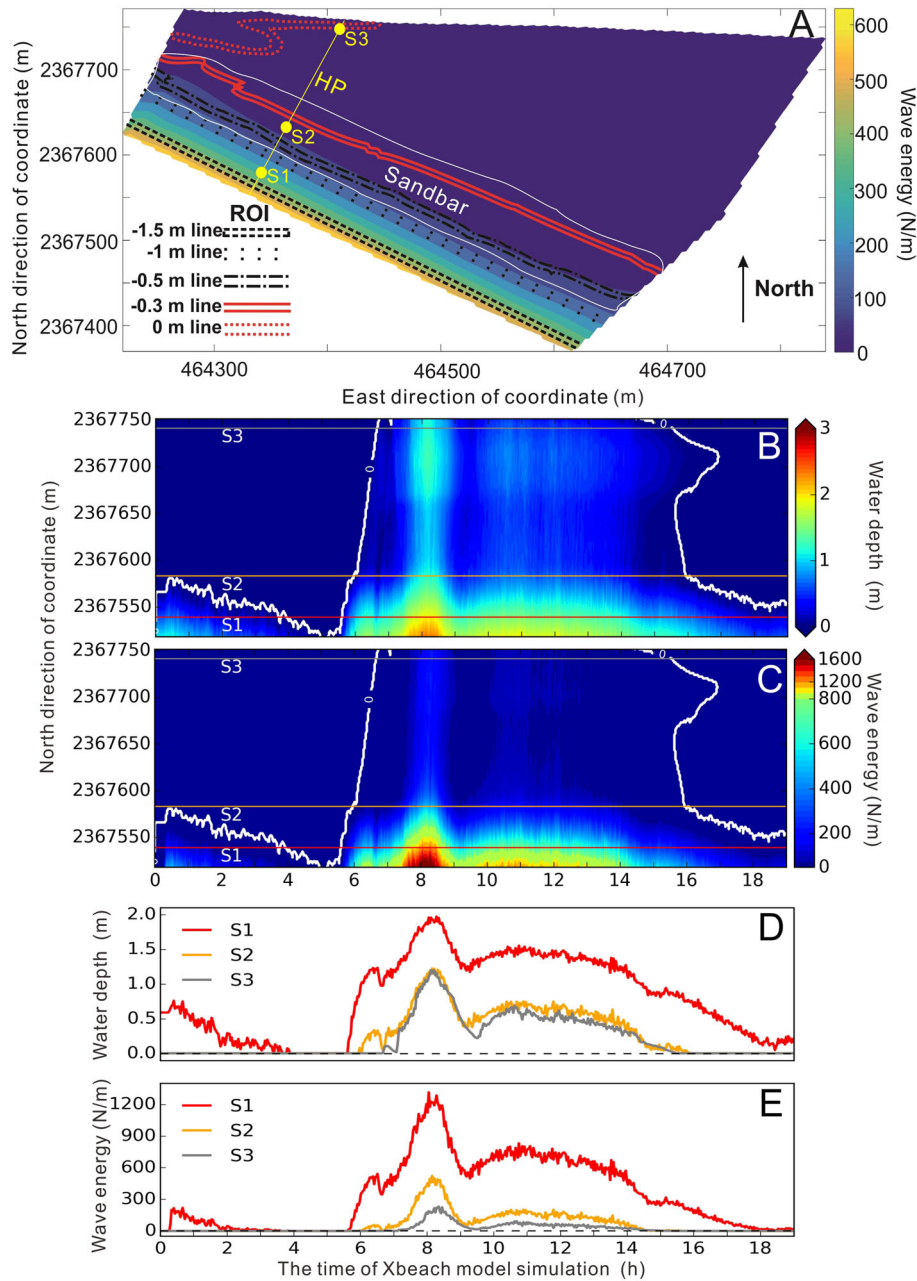


Figure 4. The wave energy in the study area during Typhoon Rammasun based on the Xbeach simulation: (A) mean wave energy in the study area and the HP profile (yellow solid line) selected in the study area – S1, S2, S3 on the profile are used for detailed presentation of the wave simulation; (B) time series of the water depth; (C) time series of the wave energy – the locations of S1, S2, S3 are shown in the figure and the white solid lines in (B, C) are zero contours; (D) time series of the water depth; (E) time series of the wave energy.

m, which is located near to the 0 m contour, and represents the backshore of the beach.

As shown in Figures 4B–E, the seawater gradually went up to the beach due to the rising tide level after the numerical simulation was conducted for approximately 6 h. When the numerical simulation was carried out for approximately 7.5 h, the seawater crossed the sandbar and entered into the backshore of the beach. After the numerical simulation was carried out for approximately 15 h, the seawater gradually receded from the beach. Before the first 6 h of the numerical simulation, there was almost no wave energy in S2 and S3. Between 6 and 7.5 h, due to the presence of an intertidal sandbar, the wave could only propagate into S2 and S3 from the east side by diffraction, so there was low wave energy in S2 and S3. After 7.5 h, with the help of the rising tide, the waves could propagate directly into S2 and S3, and as a result, the wave energy of S2 and S3 increased substantially. In addition, the wave energy of S1 was always substantially stronger than that of S2 and S3 during

the numerical simulation, and the wave energy of S2 was stronger than that of S3 during most of the simulation time.

The changes in water depth and wave energy along the HP (from S1 to S3, Figure 4A) clearly showed diminishing wave energy in the cross-shore direction of the beach. The topography of the beach, especially the intertidal sandbar, caused wave shoaling, breaking, and swash. As a result, the spatial distribution of the mean wave energy on the beach showed that the surf zone suffered the severest wave energy, the swash zone took moderate wave energy, and the backshore experienced the lowest wave energy (Figure 4A). Based on the Xbeach model, the AWEPCs of different contours in different beach zones of Yintan Beach are shown in Table III. In addition, the detailed descriptions of the varying hydrodynamic conditions in the other two beaches can be found in Archetti and Romagnoli (2011) and Aagaard *et al.* (2005); here, only the wave energy data were cited or calculated from these two studies (Tables IV and V). We aim to explore the general links

Table III. The wave energy for five regions of interest in Yintan Beach during Typhoon Rammasun

Region of interest	AWEPCC ($N m^{-1}$)	
-1.5 m	415	Figure 6A
-1 m	216	Figure 6B
-0.5 m	89	Figure 6C
-0.3 m	56	Figure 6D
0 m	11	Figure 6E

Table IV. The wave energy flux of the different storm events in Lido di Dante (data cited from Archetti and Romagnoli, 2011)

Date	Wave energy flux ($Kg * m s^{-3}$)	
10Nov 07–26Nov 07	890 370	Figure 6F
25Dec 04–21Jan 05	425 320	Figure 6G
02Apr 08–03May 08	382 450	Figure 6H
01Oct 08–12Nov 08	200 712	Figure 6I
18Apr 04–08May 04	76 263	Figure 6J

Table V. The wave energy of the different days in Egmond (data calculated from Aagaard *et al.*, 2005 and European Centre for Medium-Range Weather Forecasts)

Date	Average wave energy ($N m^{-1}$)	
24Oct 02–29Oct 02	22 262	Figure 6K
29Oct 02–30Oct 02	5048	Figure 6L
22Oct 02–24Oct 02	1971	Figure 6M
21Oct 02–22Oct 02	1262	Figure 6N
15Oct 02–21Oct 02	807	Figure 6O

between the contour/shoreline changes and the corresponding wave energy environments hereinafter.

Contour/shoreline changes in the three regions

During Typhoon Rammasun, the net sediment volume change based on survey data is approximately $-1030 m^3$ (accretion + erosion), with obvious advances and retreats in different contours, and the total volume change is $5348 m^3$ (laccretionl + lerosionl). These changes imply that Typhoon Rammasun had induced substantial sediment movement over the whole beach face. On 17 July, a channel emerged on the foreshore with two small ridges surrounding it (Figure 5A). On 20 July, the swash zone (-0.5 and -0.3 m contours located in this zone) and backshore (0 m contour located in this zone) exhibited as a flat plain with no obvious channel ridge or sandbar crest (Figure 5B). The sandbar crest was washed away by the typhoon, with an average elevation change of -8 cm. Relatively small morphological changes, mostly ranging from -2 to 2 cm, occurred on the backshore. The severest erosion occurred in the surf zone (-1.5 and -1 m contours located in this zone), with an average elevation change of -10 cm (Figures 2A–E). Regarding the erosion and accretion intensity of the different beach zones, the -1.5 m contour and its close vicinity were characterized by the severest erosion, and the -1 m contour was located in the landward direction of this severe erosion region. Most of the -0.3 m contour was located in the erosion zone, while most of the -0.5 m contour was located in the accretion zone (Figures 2C and D). Most of the 0 m contour experienced slight morphological changes, except for very few areas experiencing accretion over 0.15 m (Figure 2E).

Additionally, the frequency distributions for the absolute changes of different contours (based on field data) are shown in Figure 6. Both the -1.5 and -1 m beach elevation contour changes follow a Gaussian distribution (GD), which suffers from large AWEPCCs of 415 and $216 N m^{-1}$, respectively (Table III). The value of μ for the -1.5 m contour is larger than that for the -1 m contour, which indicates a higher sensitivity of beach elevation contour changes and weaker sediment resistance under a higher wave energy environment. Changes in the 0 m contour under the smallest AWEPCC of $11 N m^{-1}$ follow a power law (PL). In addition, both the changes of the -0.3 and -0.5 m contours, which are subject to moderate AWEPCCs of 56 and $89 N m^{-1}$ (Table III), respectively, fall into an intermediate between the logarithmic and Gaussian distributions (ILGD). The value of μ for the -0.3 m contour is smaller than that for the -0.5 m contour, demonstrating low sensitivity of beach elevation contour changes and stronger sediment resistance under a lower wave energy environment. Hence, the five sets of contour changes (-1.5 , -1 , -0.5 , -0.3 , and 0 m contours) under different wave energy environments (from 415 to $11 N m^{-1}$) quantitatively demonstrate that the frequency distribution of the beach elevation contour changes shift from GD to ILGD and finally to PL as the AWEPCC for the corresponding regions of interest decreases gradually from a high wave energy environment to a low wave energy environment.

The frequency distributions of different contour changes in Yintan Beach (meso-macrotidal beach) shift with variations in wave energy environments. The shoreline changes in Lido di Dante (microtidal and armoured beach) and Egmond (microtidal beach) also present the same characteristics of shifting frequency distributions. With decreasing wave energy, the frequency distributions of the shoreline changes in both Lido di Dante and Egmond also shift from GD to ILGD and finally to PL (Figures 6F–J and Table IV; Figures 6K–O and Table V). In addition, this consistent phenomenon of three different beaches with different tidal ranges indicates that the linear decrease in wave energy does not cause a linear decrease in contour/shoreline changes, and there must be non-linear coupling generated by morphodynamic feedbacks.

Simulation results of the conceptual model

This conceptual model is used to examine how beach contours respond to wave energy environments. High wave energy environments ($b = 0.25$) yield a frequency distribution of contour changes following a GD; this is consistent with that of the -1.5 and -1 m contours under large AWEPCCs (415 and $216 N m^{-1}$) in the field data (Figures 6A and B, 7A, Table III). As the wave energy environment decreases to moderate levels ($b = 0.16$ and 0.13), the frequency distributions of the contour changes present ILGD; this is consistent with those of the -0.5 and -0.3 m contours under moderate wave energy environments (AWEPCC = 89 and $56 N m^{-1}$, respectively) in the field data (Figures 6C and D, 7B and C). The frequency distribution of the beach elevation contour changes presents PL in response to a low wave energy environment of $b = 0.11$, which is consistent with that of the 0 m contour under a small AWEPCC of $11 N m^{-1}$ in the field data (Figures 6E and 7D).

The duration of the typhoon impact for a region is also one of the leading factors controlling morphological changes in that region (Masselink and van Heteren, 2014). T represents the total number of time steps required to approach the maximum erosion in the conceptual model of beach contour change; it increases with a decrease in b , which means that beach elevation contour changes are insensitive under a low wave energy environment, thus requiring a longer time to accomplish the



Figure 5. Photos of Yintan Beach on (A) 17 July and (B) 20 July (before and after Typhoon Rammasun), respectively.

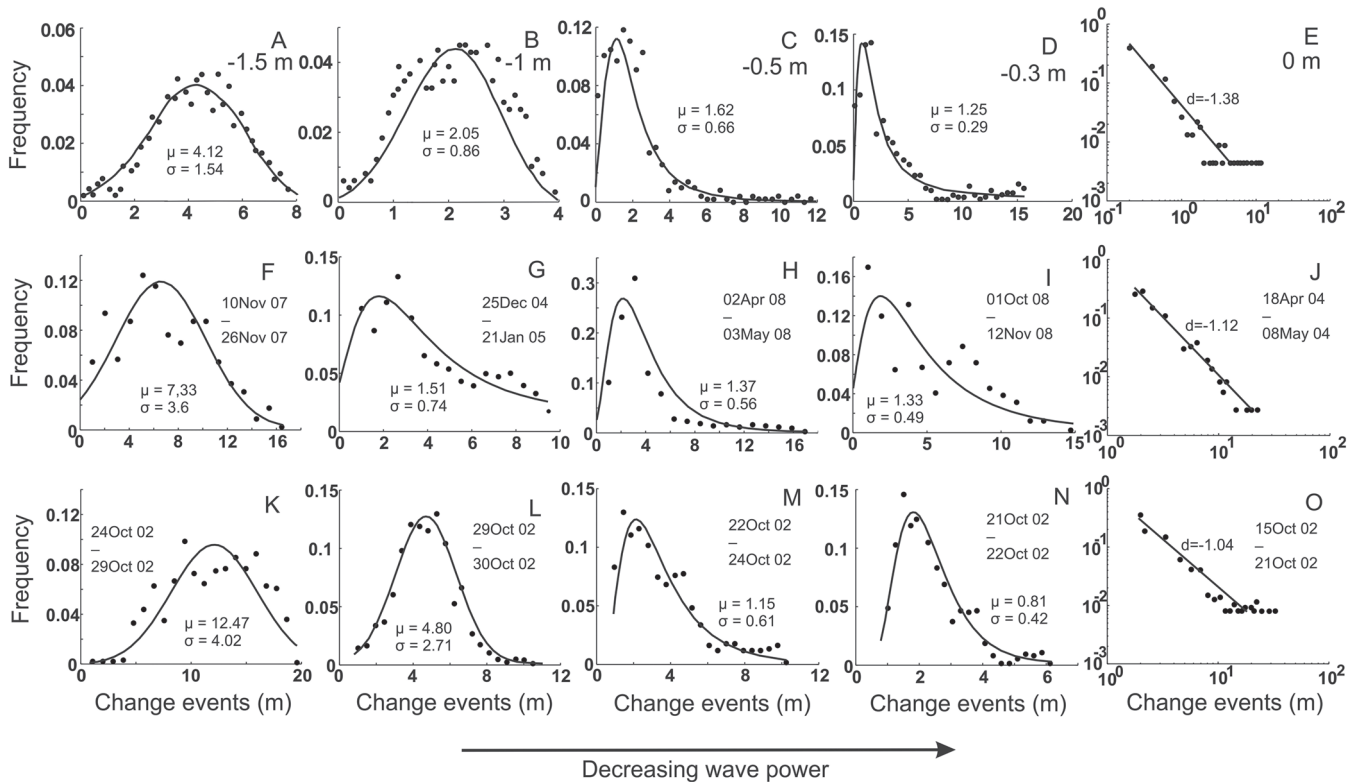


Figure 6. Frequency distributions of the observed beach elevation contour changes: (A–E) induced by Typhoon Rammasun on Yintan Beach; (F–J) induced by the different storms in Lido di Dante; (K–O) between the different days in Egmond. The wave energy of each panel can be found in Tables III–V; (A, B, F, K) follow a GD and μ, σ are the mean and standard deviation of GD; (C, D, G–I, L–N) fall into ILGD and μ, σ are the parameters of ILGD; (E, J, O) follow PL and d is the slope.

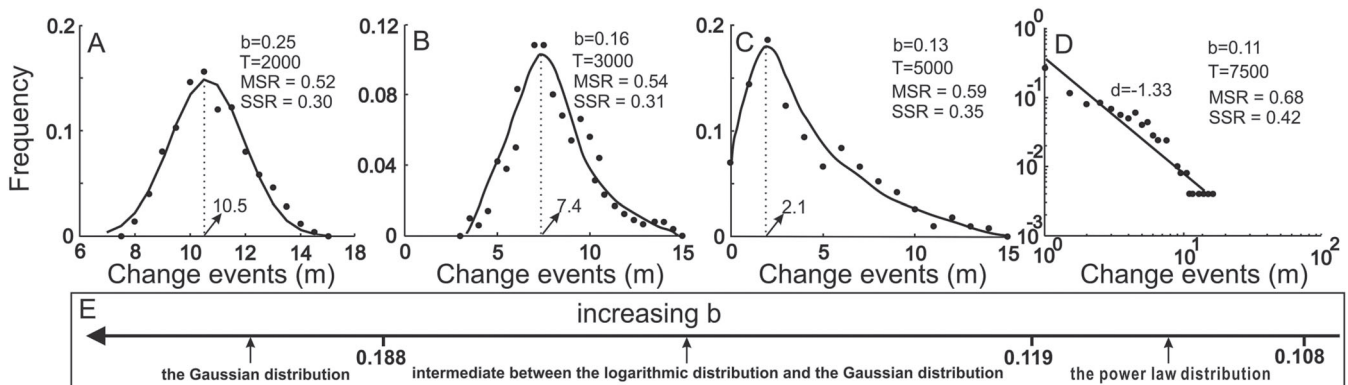


Figure 7. Frequency distributions of the contour changes based on the conceptual model results under different conditions of b : (A) follows a GD; (B, C) follow the ILGD; (D) follows PL and d is the slope; (E) shows the sensitivity of the model results to b . Other relevant parameters include: $\epsilon_1 = 1, \epsilon_2 = 0.01, k_1 = 0.002, k_2 = 0.005, dx = 1 \text{ m}, dt = 0.05 \text{ s}$.

maximum erosion. In addition, the mean η (MSR) increases with a decrease in the wave energy (Figure 7), implying that sediment resistance under a low wave energy environment is obviously stronger than that under a high wave energy environment, which is consistent with the results from the field data (Figures 6A–E). Moreover, with the fixed contour erosion of 15 m, a decrease in b of 0.09 (from $b = 0.25$ to 0.16) yields an increase in T of 1000 (Figures 7A and B), while a decrease in b of 0.02 (from $b = 0.13$ to 0.11) yields a corresponding increase in T of 2500 (Figures 7C and D). Although the trend is monotonous, such that T increases with a decrease in b , the relationship between the increase in T and the decrease in b is nonlinear. Furthermore, both the upper and lower limits of the local sediment resistance (SSR) increase with decreasing wave energy (Figure 7), suggesting that high wave energy tends to create more homogeneous local sediment resistance, whereas low wave energy tends to create more heterogeneous local sediment resistance.

Discussion

Frequency distributions of the beach elevation contour changes under different wave energy environments

The frequency distributions of beach elevation contour changes induced by typhoons show distinct behaviours in different beach zones that are subject to different wave energy strengths. According to the field data, after Typhoon Rammasun –1.5 and –1 m contours that are under high wave energy environments remain as straight configurations (Figures 2A and B), while the 0 m contour under a low wave energy environment exhibits a curved contour configuration with slight changes for most parts but drastic changes for the rest of the parts (Figure 2E). As a result, the frequency distributions of beach elevation contour changes show GD in the surf zone (–1.5 and –1 m contours) of high wave energy environments (AWEPC = 415 and 216 N m^{-1} , respectively), ILGD in the swash zone (–0.5 and –0.3 m contours) of moderate wave energy environments (AWEPC = 89 and 56 N m^{-1} , respectively), and PL in the backshore (0 m contour) of low wave energy environments (AWEPC = 11 N m^{-1}) (Figures 6A–E, Table III). In addition, the frequency distributions of shoreline changes in the other two different beaches

present identical characteristics under different wave energy environments (Figures 6F–O). Moreover, the conceptual model results indicate that the erosive ability of waves (relative magnitude of b) controls the frequency distribution of the contour changes (Figure 7E). Specifically, for a large b (over 0.188), the frequency distribution of the contour changes follows a GD; for a moderate b (from 0.119 to 0.188), the frequency distribution falls into ILGD; for b between 0.108 and 0.119, the frequency distribution presents a PL feature. Hence, it is inferred that the frequency distributions of the beach elevation contour changes exhibit distinct features under different wave energy environments (i.e. a high wave energy generates a GD and a moderate wave energy induces an ILGD, while a low wave energy produces a PL of contours/shoreline changes).

Sediment resistance in response to different wave energy environments

The relative importance of the internal processes due to sediment and the external processes is a critical factor for beach elevation contour changes in different beach zones (Dai *et al.*, 2018). According to the results of the conceptual model and the field data of Yintan Beach, changes in the –1.5 m contour (under a high wave energy environment) are the most severe, while those of the 0 m contour (under a low wave energy environment) are slight after the typhoon. Moreover, the sediment resistance increases gradually and becomes more heterogeneous with a decrease in the wave energy (Figure 6 and MSR, SSR of Figures 7A–D). Thus, it is indicated that beach elevation contour changes under high wave energy environments are dominated by external processes (i.e. wave energy), while those under low wave energy environments are dominated by the internal processes due to sediment (i.e. sediment resistance). For those under moderate wave energy environments, they are dual-controlled by both the internal processes due to sediment and external processes. The increasing relative importance of sediment resistance is attributed to the transformation of the bedform morphology. With the combination of waves and water depth from the Xbeach model, the mean sediment mobility numbers ψ at S1, S2, and S3 are calculated as 410, 190, and 35 (Figure 8A), respectively. Therefore, the corresponding bedforms are dominated by a plane seabed (Figure 9C), post-vortex ripples (Figure 9B), and vortex ripples

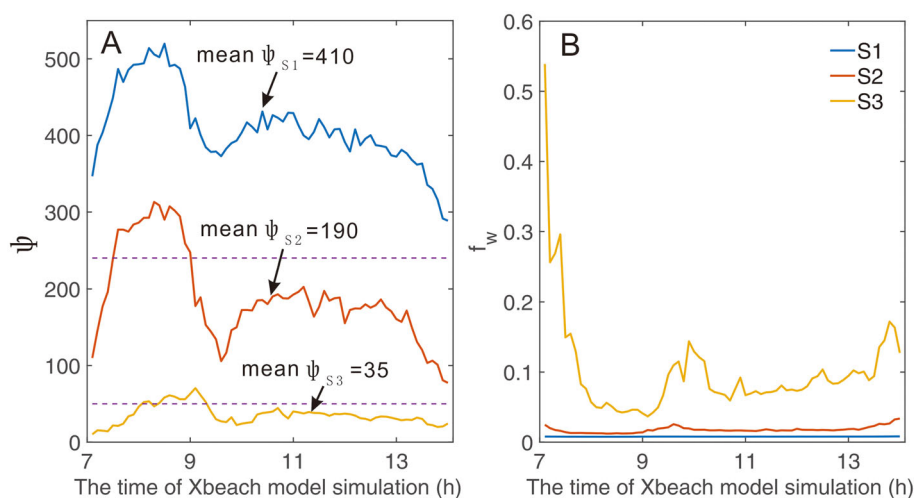


Figure 8. Simultaneous variations of (A) mobility number (ψ) and (B) wave friction factor (f_w) against the time of the Xbeach model simulation (h) during Typhoon Rammasun at S1 (blue lines), S2 (red lines), and S3 (yellow lines). Note that the two purple dashed lines in (A) ($\psi = 50$ and 240) correspond to the boundary between the vortex ripple and post-vortex ripple, and between the post-vortex ripple and plane seabed, respectively.

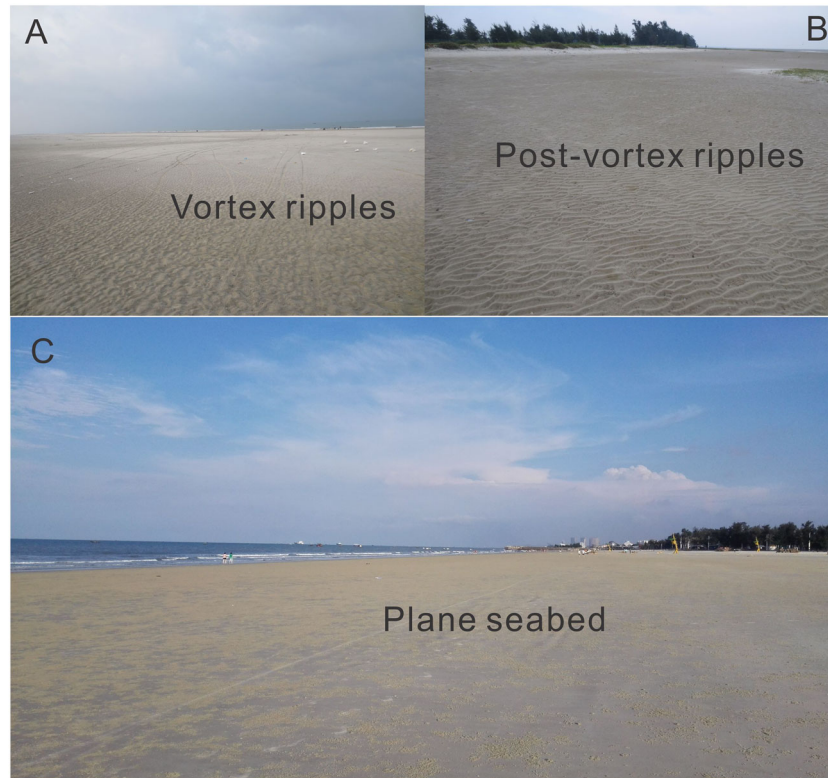


Figure 9. The bedforms are dominated by (A) vortex ripples under a low wave energy environment; (B) post-vortex ripples under a moderate wave energy environment; and (C) a plane seabed under a high wave energy environment.

(Figure 9A) (Dingler and Inman, 1976; Nielsen, 1981) during the typhoon. As a result, the wave friction factor f_w , a coefficient reflecting the sediment resistance against wave erosion and causing wave energy dissipation (Jonsson, 1966) due to the formation of sand ripples induced by near-bed wave orbital motions, reaches the largest value at S3, where a low wave energy environment prevails, followed by that at S2. The smallest f_w occurs at S1, where the seabed is planar under a high wave energy environment (Figure 8B). The reduction in f_w is caused by a decrease in seabed roughness and an increase in wave energy, which is consistent with previous work (Smyth and Hay, 2002). In other words, variations in both the sediment resistance and seabed roughness showed negative relations with the wave energy. This explains why the sediment resistance is strong and heterogeneous under a low wave energy environment but is relatively weak and homogeneous under a high wave energy environment, which also provides evidence for the simulation results from the conceptual model of beach elevation contour changes.

Conclusions

Beaches are important resources for leisure and entertainment, coastal protection and aquaculture, but little attention is given to the behaviour of beach elevation contours in response to different wave energy environments. By analysing the collected and measured beach elevation contours/shorelines and wave energy data from three international beaches, plus the wave energy data simulated by Xbeach in Yintan Beach, it is demonstrated that beach contour/shoreline changes under different wave energy environments follow distinct frequency distributions. A high wave energy environment induces GD of contours/shoreline changes; a moderate wave energy environment induces ILGD; and a low wave energy environment induces PL. A conceptual model illustrated that the relative

importance of the internal processes due to sediment (i.e. sediment resistance) and external processes (i.e. wave energy) determines the way that beach elevation contours evolve under different wave energy environments. Hence, we suggest that more work needs to be conducted on the relation between beach elevation contour changes and the corresponding 3D geomorphic evolution in the future.

Acknowledgements, Samples, and Data

This study was supported by the State Key Program of National Natural Science of China (41930537) and National Natural Science Foundation of China (NSFC) (41666003, 41376097). The hydrological data of Yintan Beach are available from China Oceanic Information Network (<http://www.coi.gov.cn/>). Z. Dai conceived this research. W. Pang, Z. Ge, and S. Li conducted the field observations. W. Pang, Z. Dai, and Z. Ge carried out the main data analysis. W. Pang, Z. Dai, and Z. Ge wrote the article. Z. Dai, S. Li, and H. Huang contributed to the discussion.

Conflict of Interest

The authors declare no conflict of interest.

Data Availability Statement

The datasets used and/or analysed during the current study are available from the corresponding author on reasonable request.

References

- Aagaard T, Kroon A, Andersen S, Møller Sørensen R, Quartel S, Vinther N. 2005. Intertidal beach change during storm conditions; Egmond, The Netherlands. *Marine Geology* **218**: 65–80. <https://doi.org/10.1016/j.margeo.2005.04.001>
- Anderson TR, Frazer LN, Fletcher CH. 2010. Transient and persistent shoreline change from a storm. *Geophysical Research Letters* **37**: 162–169. <https://doi.org/10.1029/2009GL042252>
- Anthony EJ. 2008. Chapter five sandy beaches and barriers. *Developments in Marine Geology* **4**: 159–288. [https://doi.org/10.1016/S1572-5480\(08\)00405-3](https://doi.org/10.1016/S1572-5480(08)00405-3)
- Archetti R, Romagnoli C. 2011. Analysis of the effects of different storm events on shoreline dynamics of an artificially embayed beach. *Earth Surface Processes and Landforms* **36**: 1449–1463. <https://doi.org/10.1002/esp.2162>
- Ashton A, Murray AB, Arnault O. 2001. Formation of coastline features by large-scale instabilities induced by high-angle waves. *Nature* **414**: 296–300. <https://doi.org/10.1038/35104541>
- Boak EH, Turner IL. 2005. Shoreline definition and detection: a review. *Journal of Coastal Research* **21**(4): 688–703. <https://doi.org/10.2112/03-0071.1>
- Bonaldo D, Antonioli F, Archetti R, Bezzi A, Correggiari A, Davolio S, de Falco G, Fantini M, Fontolan G, Furlani S, Gaeta MG, Leoni G, Lo Presti V, Mastronuzzi G, Pillon S, Ricchi A, Stocchi P, Samaras AG, Scicchitano G, Carniel S. 2019. Integrating multidisciplinary instruments for assessing coastal vulnerability to erosion and sea level rise: lessons and challenges from the Adriatic Sea, Italy. *Journal of Coastal Conservation* **23**: 19–37. <https://doi.org/10.1007/s11852-018-0633-x>
- Corbella S, Stretch DD. 2012. Predicting coastal erosion trends using non-stationary statistics and process-based models. *Coastal Engineering* **70**: 40–49. <https://doi.org/10.1016/j.coastaleng.2012.06.004>
- Dai Z, Fagherazzi S, Gao S, Mei X, Ge Z, Wei W. 2018. Scaling properties of estuarine beaches. *Marine Geology* **404**: 130–136. <https://doi.org/10.1016/j.margeo.2018.07.011>
- Dawson JL, Smithers SG. 2010. Shoreline and beach volume change between 1967 and 2007 at Raine Island, Great Barrier Reef, Australia. *Global and Planetary Change* **72**: 141–154. <https://doi.org/10.1016/j.gloplacha.2010.01.026>
- Dean RG, Dalrymple RA. 2004. *Coastal Processes with Engineering Applications*. Cambridge University Press: Cambridge, UK.
- Defeo O, McLachlan A, Schoeman DS, Schlacher T, Dugan J, Jones A, Lastra M, Scapini F. 2009. Threats to sandy beach ecosystems: a review. *Estuarine, Coastal and Shelf Science* **81**: 1–12. <https://doi.org/10.1016/j.ecss.2008.09.022>
- Dingler JR, Inman DL. 1976. Wave-formed ripples in nearshore sands. *Coastal Engineering Proceedings* **1**(15): 122–139. <https://doi.org/10.9753/icce.v15.122>
- Fagherazzi S, Carniello L, D'Alpaos L, Defina A. 2006. Critical bifurcation of shallow microtidal landforms in tidal flats and salt marshes. *Proceedings of the National Academy of Sciences of the United States of America* **103**: 8837–8841. <https://doi.org/10.1073/pnas.0508379103>
- Garnier R, Calvete D, Falqués A, Caballeria M. 2006. Generation and nonlinear evolution of shore-oblique/transverse sand bars. *Journal of Fluid Mechanics* **567**: 327–360. <https://doi.org/10.1017/S0022112006002126>
- Ge Z, Dai Z, Pang W, Li S, Wei W, Mei X, Huang H, Gu J. 2017. LIDAR-based detection of the post-typhoon recovery of a meso-macro-tidal beach in the Beibu Gulf, China. *Marine Geology* **391**: 127–143. <https://doi.org/10.1016/j.margeo.2017.08.008>
- Hinkel J, Jaeger C, Nicholls RJ, Lowe J, Renn O, Peijun S. 2015. Sea level rise scenarios and coastal risk management. *Nature Climate Change* **5**: 188–190. <https://doi.org/10.1038/nclimate2505>
- Jonsson IG. 1966. Wave boundary layers and friction factors. In *Proceedings of the 10th International Conference on Coastal Engineering*, Tokyo, Japan; 127–148. <https://doi.org/10.1061/9780872620087.010>
- Kraus NC, Harikai S. 1983. Numerical model of the shoreline change at Oarai Beach. *Coastal Engineering* **7**(1): 1–28. [https://doi.org/10.1016/0378-3839\(83\)90024-8](https://doi.org/10.1016/0378-3839(83)90024-8)
- Kroon A, Aarninkhof SGJ, Archetti R, Armaroli C, Gonzalez M, Medri S, Osorio A, Aagaard T, Davidson MA, Holman RA, Spanhoff R. 2007. Application of remote sensing video systems for coastline management problems. *Coastal Engineering* **54**(6–7): 493–505. <https://doi.org/10.1016/j.coastaleng.2007.01.004>
- Leonardi N, Fagherazzi S. 2014. How waves shape salt marshes. *Geology* **42**(10): 887–890.
- Leonardi N, Fagherazzi S. 2015. Effect of local variability in erosional resistance on large-scale morphodynamic response of salt marshes to wind waves and extreme events. *Geophysical Research Letters* **42**: 5872–5879. <https://doi.org/10.1002/2015GL064730>
- Lippmann TC, Holman RA. 1989. Quantification of sand bar morphology: a video technique based on wave dissipation. *Journal of Geophysical Research, Oceans* **94**(C1): 995–1011. <https://doi.org/10.1029/JC094iC01p00995>
- Masselink G, van Heteren S. 2014. Response of wave-dominated and mixed-energy barriers to storms. *Marine Geology* **352**: 321–347. <https://doi.org/10.1016/j.margeo.2013.11.004>
- McCall RT, de Vries JVT, Plant NG, van Dongeren AR, Roelvink JA, Thompson DM, Reniers AJHM. 2010. Two-dimensional time dependent hurricane overwash and erosion modeling at Santa Rosa Island. *Coastal Engineering* **57**: 668–683. <https://doi.org/10.1016/j.coastaleng.2010.02.006>
- Nielsen P. 1981. Dynamics and geometry of wave-generated ripples. *Journal of Geophysical Research-Atmospheres* **86**(C7): 6467–6472. <https://doi.org/10.1029/JC086iC07p06467>
- Nordstrom KF. 2000. *Beaches and Dunes on Developed Coasts*. Cambridge University Press: Cambridge, UK.
- Quartel S, Kroon A, Ruessink BG. 2008. Seasonal accretion and erosion patterns of a microtidal sandy beach. *Marine Geology* **250**: 19–33. <https://doi.org/10.1016/j.margeo.2007.11.003>
- Roelvink D, Reniers A, van Dongeren A, de Vries JVT, McCall R, Lescinski J. 2009. Modelling storm impacts on beaches, dunes and barrier islands. *Coastal Engineering* **56**: 1133–1152. <https://doi.org/10.1016/j.coastaleng.2009.08.006>
- Short AD. 1979. Three dimensional beach stage model. *Journal of Geology* **87**: 553–571. <https://doi.org/10.1086/628445>
- Smith RK, Bryan KR. 2007. Monitoring beach face volume with a combination of intermittent profiling and video imagery. *Journal of Coastal Research* **23**(4): 892–898. <https://doi.org/10.2112/04-0287.1>
- Smyth C, Hay AE. 2002. Wave friction factors in nearshore sands. *Journal of Physical Oceanography* **32**(12): 3490–3498. [https://doi.org/10.1175/1520-0485\(2002\)0322.0.CO;2](https://doi.org/10.1175/1520-0485(2002)0322.0.CO;2)
- Splinter KD, Turner IL, Reinhardt M, Ruessink G. 2017. Rapid adjustment of shoreline behavior to changing seasonality of storms: observations and modelling at an open-coast beach. *Earth Surface Processes and Landforms* **42**(8): 1186–1194. <https://doi.org/10.1002/esp.4088>
- Stive M. 2004. How important is global warming for coastal erosion. *Climatic Change* **64**: 27–39. <https://doi.org/10.1023/B:CLIM.0000024785.91858.1d>
- Swart DH. 1974. A schematisation of onshore-offshore transport. In *Proceedings of the 14th International Conference on Coastal Engineering Copenhagen, Denmark*; 1782–1798. <https://doi.org/10.1061/9780872621138.054>
- Theuerkauf EJ, Rodriguez AB. 2014. Evaluating proxies for estimating subaerial beach volume change across increasing time scales and various morphologies. *Earth Surface Processes and Landforms* **39**(5): 593–604. <https://doi.org/10.1002/esp.3467>
- Thieler ER, Himmelstoss EA, Zichichi JL, Ergul A. 2009. Digital Shoreline Analysis System (DSAS) version 4.0 – an ArcGIS extension for calculating shoreline change. U.S. Geological Survey Open-File Report 2008-1278. * Current version 4.3.
- Winterwerp JC, van Kesteren WGM. 2004. *Introduction to the Physics of Cohesive Sediment in the Marine Environment*. Elsevier: Amsterdam.

- Yates ML, Guza RT, O'Reilly WC. 2009. Equilibrium shoreline response: observations and modeling. *Journal of Geophysical Research Oceans* **114**(C09014): 1–16. <https://doi.org/10.1029/2009JC005359>
- Yu F, Switzer AD, Lau AYA, Yeung HYE, Chik SW, Chiu HC, Huang Z, Pile J. 2013. A comparison of the post-storm recovery of two sandy beaches on Hong Kong Island, southern China. *Quaternary International* **304**: 163–175. <https://doi.org/10.1016/j.quaint.2013.04.002>

Supporting Information

Additional supporting information may be found online in the Supporting Information section at the end of the article.

Data S1 Supporting Information